

In the format provided by the authors and unedited.

Quantum spin liquids unveil the genuine Mott state

A. Pustogow ^{1*}, M. Bories¹, A. Löhle¹, R. Rösslhuber¹, E. Zhukova², B. Gorshunov², S. Tomić³, J. A. Schlueter^{4,5}, R. Hübner ^{1,6}, T. Hiramatsu⁷, Y. Yoshida^{7,8}, G. Saito^{7,9}, R. Kato¹⁰, T.-H. Lee¹¹, V. Dobrosavljević¹¹, S. Fratini ¹² and M. Dressel¹

¹Physikalisches Institut, Universität Stuttgart, Stuttgart, Germany. ²Moscow Institute of Physics and Technology (State University), Dolgoprudny, Russia. ³Institut za fiziku, Zagreb, Croatia. ⁴Division of Materials Research, National Science Foundation, Arlington, VA, USA. ⁵Materials Science Division, Argonne National Laboratory, Argonne, IL, USA. ⁶Biomedizinische Chemie, Institut für Klinische Radiologie und Nuklearmedizin, Universität Heidelberg, Mannheim, Germany. ⁷Faculty of Agriculture, Meijo University, Nagoya, Japan. ⁸Division of Chemistry, Graduate School of Science, Kyoto University, Kyoto, Japan. ⁹Toyota Physical and Chemical Research Institute, Nagakute, Japan. ¹⁰Condensed Molecular Materials Laboratory, RIKEN, Wako-shi, Saitama, Japan. ¹¹Department of Physics and National High Magnetic Field Laboratory, Florida State University, Tallahassee, FL, USA. ¹²Institut Néel – CNRS and Université Grenoble Alpes, Grenoble, France. *e-mail: andrej.pustogow@pi1.physik.uni-stuttgart.de

Supplementary Information

Quantum Spin Liquids Unveil the Genuine Mott State

A. Pustogow*, M. Bories, A. Löhle, R. Rösslhuber, E. Zhukova, B. Gorshunov, S. Tomić, J.A. Schlueter, R. Hübner, T. Hiramatsu, Y. Yoshida, G. Saito, R. Kato, T.-H. Lee, V. Dobrosavljević, S. Fratini and M. Dressel

Parts of the text and results reported in this work have been reproduced from the thesis of A.P., at the University of Stuttgart, and accessible at <http://dx.doi.org/10.18419/opus-9487> [S31].

S1 Band Parameters: Definitions

Strictly speaking, the Coulomb interaction U referred to in the text and in Fig. 1 equates with the effective Coulomb interaction $U = U_0 - V_0$, where U_0 and V_0 are on-site and nearest-neighbour Coulomb repulsion, respectively. Upon moving an electron to its neighbouring site, a vacancy and a double occupancy are created, so-called holons and doublons. While the former reduces the nearest-neighbour repulsion, the latter enhances the on-site Coulomb energy, resulting in a total energy cost of $U = U_0 - V_0$. Empirically, the on-site term can be approximated with the strength of the intra-dimer transfer integrals $U_0 \approx 2t_d$, which is used in Table S1. There, we additionally compare the inter-dimer transfer integrals t , t' as a measure of the geometrical frustration of the spin-liquid compounds under investigation. For completeness reasons we also list those of the related charge-transfer salts κ -(BEDT-TTF)₂Cu[N(CN)₂]Cl and κ -(BEDT-TTF)₂Cu[N(CN)₂]Br; these are well-studied compounds with a significantly weaker frustration t'/t that order antiferromagnetically or become metallic and even superconducting at low temperatures, depending on the U/W ratio [S1,S2,S3,S4,S5]. The U/W ratio obtained from *ab initio* density functional theory (DFT) and extended Hückel calculations based on the respective crystal structure indicates that correlations increase considerably when going from κ -(BEDT-TTF)₂Cu₂(CN)₃ (abbreviated CuCN) via κ -(BEDT-TTF)₂Ag₂(CN)₃ (abbreviated AgCN) to β -EtMe₃Sb[Pd(dmit)₂]₂ (abbreviated EtMe), consistent with the experiments. Moreover, the bandwidth W and Coulomb repulsion U extracted from our optical experiments (Figs. 2, S7, S9) show the same trend. Deviations of the absolute value, however, stem from the limitations of the respective theoretical models.

Compound	t_d (meV)	t (meV)	t' (meV)	t'/t	U/t	$W_0 = 9t$ (meV)	U/W_0	$(U/W)_{\text{exp}}$
κ -(BEDT-TTF) ₂ Cu[N(CN) ₂] ₂ Br	200	78	33	0.42	5.1	500	0.8	
κ -(BEDT-TTF) ₂ Cu[N(CN) ₂] ₂ Cl	200	73	32	0.44	5.5	476	0.84	1.5
κ -(BEDT-TTF) ₂ Cu ₂ (CN) ₃	200	55	45	0.83	7.3	450	0.89	1.52
κ -(BEDT-TTF) ₂ Ag ₂ (CN) ₃	264	53	48	0.90	10.5	454	1.16	1.96
β '-EtMe ₃ Sb[Pd(dmit) ₂] ₂	454	28	26	0.92	32	244	3.72	2.35

Table 1. Electronic parameters of several organic charge-transfer salts with different correlation strength.

κ -(BEDT-TTF)₂Cu[N(CN)₂]₂Br is metallic and becomes superconducting below $T_c = 11.8$ K. κ -(BEDT-TTF)₂Cu[N(CN)₂]₂Cl is a Mott insulator that orders antiferromagnetically at $T_N = 25$ K; only 300 bar are sufficient to cross the insulator-to-metal transition. The spin liquid compounds κ -(BEDT-TTF)₂Cu₂(CN)₃ and κ -(BEDT-TTF)₂Ag₂(CN)₃ exhibit no magnetic order down to 20 mK, although the exchange coupling $J = 250$ K is rather strong. The coupling within the dimers t_d is a measure of the Coulomb repulsion U . The transfer integrals t and t' characterize the frustration on the triangular lattice. The relative strength of correlations is given by U/t and U/W_0 . The last column gives parameters solely determined from our optical measurements. U is experimentally determined from the mid-infrared maximum in the optical conductivity and the bandwidth W is deduced from the width of the corresponding band (cf. Figs. 2 and S7). Because W is defined from the full width at half maximum in the density of states, it constitutes a lower bound to the actual bandwidth. Together with the sizable renormalization of the bandwidth expected due to electronic correlations [S6,S7,S8], this causes the extracted U/W to be generally larger than the calculated U/W_0 [S3,S9,S10,S11,S12,S13,S14]. Table reproduced from Ref. [S31].

S2 Construction of the Phase Diagram from Pressure-Dependent dc-Transport and Optics

Making use of our conclusions from the optical spectroscopic results presented in Fig. 2 we relate the transport results of the three frustrated Mott insulators to each other and combine them to a universal quantum Widom line (QWL). In the T - p phase diagrams shown in Furukawa *et al.* [S15] the back-bending point of the QWL is located at a lower temperature for EtMe ($T_{\text{back}} < 35$ K) as compared to CuCN ($T_{\text{back}} = 70$ K) (Fig. S1). This agrees with the smaller bandwidth of EtMe providing evidence for the T/W scaling of the phase diagram. Considering that EtMe is located much deeper in the Mott insulating regime (cf. Fig. 2 **h**) it is remarkable that the pressure at the back-bending point ($p_{\text{back}} \geq 3$ kbar) is similar to CuCN, consistent with the large compressibility of EtMe concluded from optical experiments. For AgCN, a similar compressibility but larger Coulomb repulsion compared to CuCN was concluded in a very recent study [S13], also consistent with our optical results. The overall agreement between optics, pressure-dependent transport and the theoretically determined band parameters strongly encourages our T/W vs. U/W scaling approach.

Fig. S1 illustrates the scaling procedure to connect the QWL of EtMe and CuCN based on the pressure-dependent dc transport results by Furukawa *et al.* [S15] and the data shown in Figs. S2 and S13. Due to different bandwidth and electronic correlations each compound covers a distinct range in the phase diagram. Upon rescaling the temperature and pressure axes by U and W , the intrinsic Mott physics is revealed and all data points collapse on a universal quantum Widom line. A good match between the EtMe and CuCN data sets can be reached for $2 < T_{\text{EtMe}}/T_{\text{CuCN}} < 4.5$. The best fit, however, is achieved for a bandwidth ratio of 3.4, when also the normalized resistance values, i.e. the colour scale in Fig. 1 **d** and **f** from Ref. [S15], are in agreement. For AgCN, the QWL was extracted from the pressure-dependent resistivity reported in Ref. [S13] and then similarly scaled to match with the EtMe and CuCN data.

While above the QWL was determined via the largest rate of change of logarithmic resistivity upon sweeping pressure, i.e. the maximum of $d\ln(\rho)/dp$, we find indications for the crossover even upon a temperature sweep at ambient pressure. As demonstrated in Fig. S2, the transport gap $d\ln(\rho)/d(1/T)$ obtained from the Arrhenius plot of the dc resistivity acquires a broad peak at the QWL. It widens significantly on the T/W scale for larger correlations, possibly as a result of the increasing distance to the coherent regime adjacent to the low-temperature Mott transition. One may interpret this observation in a way that, in this region of the phase diagram, the Mott state competes with thermal excitations only.

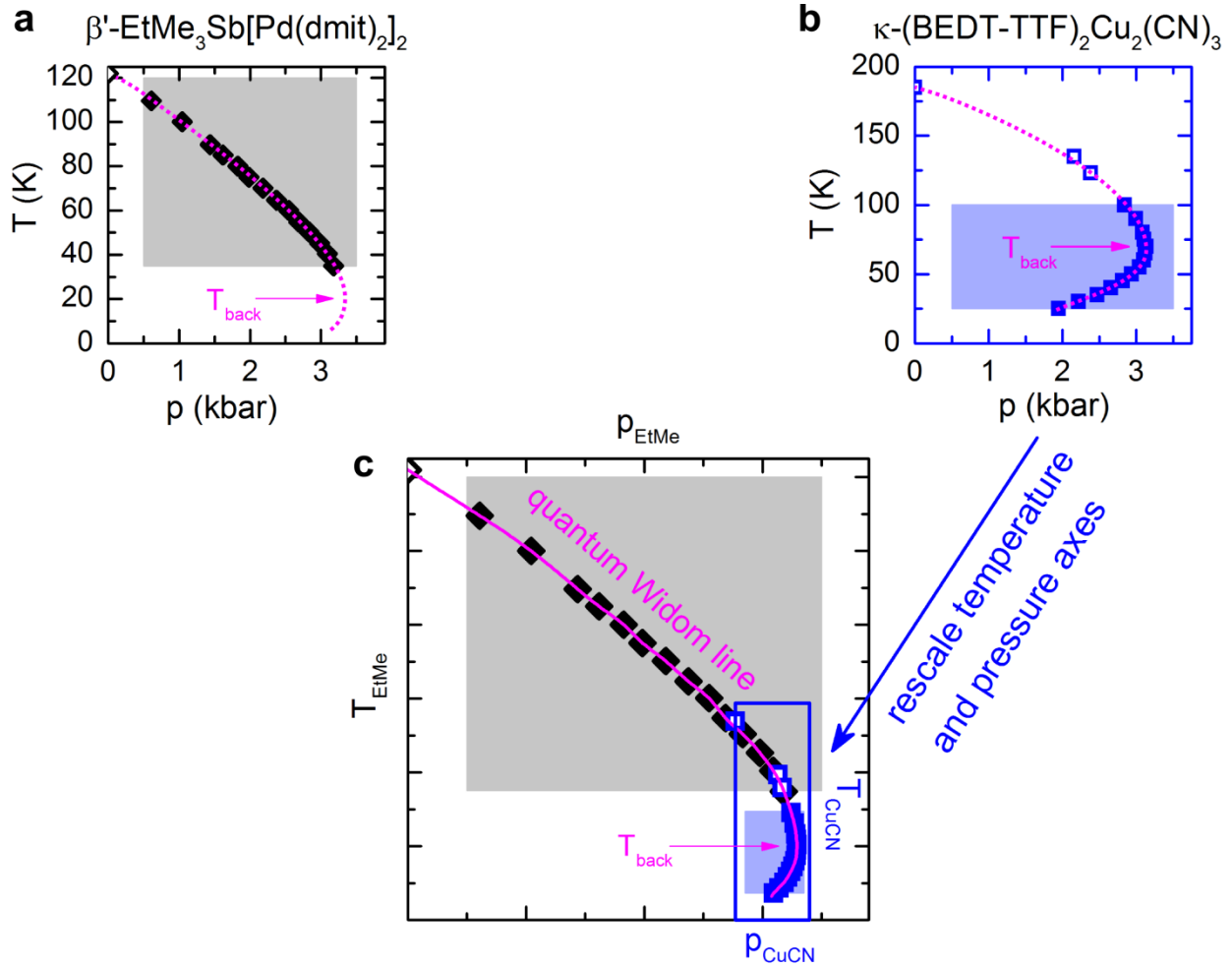


Figure S1. Rescaling procedure to connect the quantum Widom lines of β -EtMe₃Sb [Pd(dmit)₂]₂ (black) and κ -(BEDT-TTF)₂Cu₂(CN)₃ (blue).

a,b, The temperature and pressure range covered by the dc transport experiments of Furukawa *et al.* [S15] is highlighted in grey and blue, respectively; the solid symbols correspond to the quantum Widom line (QWL) determined by pressure sweeps at constant temperature. The dotted magenta lines illustrate the interpolation of the QWL. The QWL coincides with the maximum of the transport gap $\Delta(T)$ (open symbols, cf. Figs. S2 and S13 c). **c,** Using the back-bending at T_{back} as a fixed point, the two data sets can be connected smoothly by stretching and squeezing of the respective axes, resulting in a universal QWL (solid magenta line). As indicated by the blue rectangle, temperature and pressure of κ -(BEDT-TTF)₂Cu₂(CN)₃ are scaled down by factors of 3.4 and 6 compared to β -EtMe₃Sb[Pd(dmit)₂]₂, respectively. This implies that β -EtMe₃Sb[Pd(dmit)₂]₂ has a smaller bandwidth, larger compressibility and its ambient pressure position is located more *left* in the phase diagram than for κ -(BEDT-TTF)₂Cu₂(CN)₃, consistent with the optical results from Fig. 2. Figure reproduced from Ref. [S31].

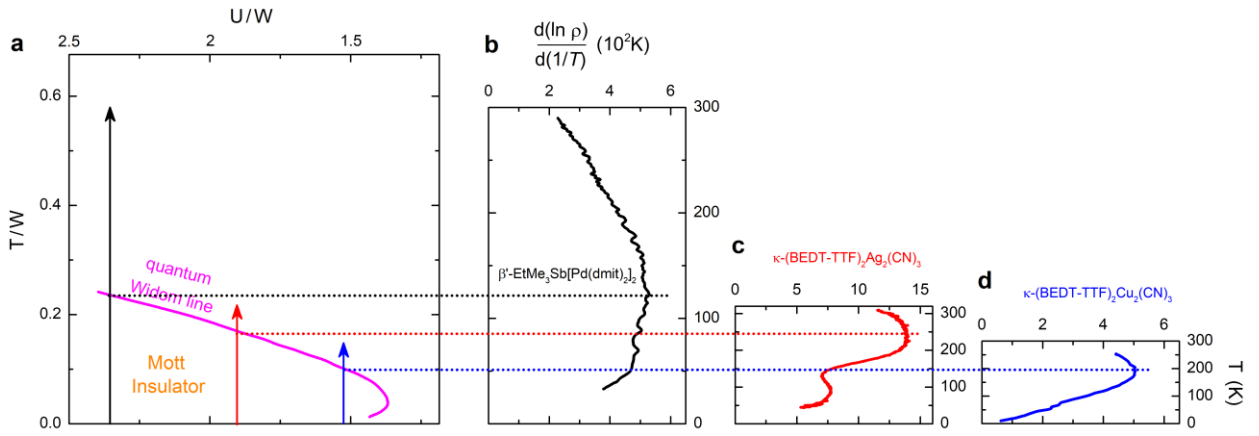


Figure S2. The transport gap acquires a maximum at the quantum Widom line. **a**, The universal quantum Widom line was assembled from the pressure-dependent dc transport data as indicated in Fig. S1. The coloured arrows correspond to the temperature range of our transport experiments renormalized by the scaling factor (Equ. S1) that accounts for the different bandwidth. **b-d**, The transport gap is derived from the logarithmic derivative with respect to inverse temperature. It acquires a broad maximum at the quantum Widom line which narrows significantly upon approaching the low-temperature Mott transition.

Taking CuCN as our reference material, we rescale the temperature and pressure of EtMe by factors 3.4 and 6, respectively; AgCN has a temperature scaling factor of 1.2 compared to CuCN, almost equal compressibility and is shifted to the left on the horizontal axis due to the larger U , in good agreement with Ref. [S13]. The ambient conditions are located at -1.66 GPa for EtMe and -0.83 GPa for AgCN on the CuCN pressure scale implying the following linear scaling relations:

$$p_{\text{CuCN}} = -0.83\text{GPa} + 0.95p_{\text{AgCN}} = -1.66\text{GPa} + 6p_{\text{EtMe}}. \quad (\text{S1})$$

Due to the different experimental approach of Shimizu *et al.* [S13], who measured temperature sweeps at constant pressure rather than pressure sweeps at constant temperature, the QWL determination was not as accurate for AgCN, as indicated by the error bars in Fig. S8. Note that they concluded an absolute pressure shift of 0.6 GPa between AgCN and CuCN while our procedure results in a shift of approximately 0.8 GPa, as shown in Equ. S1. Their assumption, however, is based on pressure-dependent transport studies of CuCN employing oil as pressure medium [S17]. It is known that such setups suffer from a pressure loss at low temperatures when the oil freezes, making the pressure determination at low temperatures less accurate. On the other hand, the data of Furukawa *et al.* [S15] on CuCN were measured in a He gas cylinder where the applied pressure can be adjusted and determined very accurately even at low

temperatures. This explains the different pressure scale compared to Kurosaki *et al.* [S17], where superconductivity sets in at 0.35 GPa while the insulator-superconductor phase boundary of CuCN is located at 0.125 GPa in Ref. [S15].

The unified phase diagram presented in Fig. 4 based on the bandwidth W and Coulomb repulsion U determined by optical spectroscopy (cf. Fig. 2, Fig. S9) shows excellent agreement between the optical and transport investigations. Comparing the experimental QWL (Fig. 4) with the dynamical mean field theory (DMFT) calculations employing the iterated perturbation theory solver (Fig. 1 **a**) yields similar U/W_0 values at the reversal point. Therefore, the critical correlations needed to drive the metal into a Mott insulator are reproduced very well. Also the vertical position of the QWL, i.e. the optically determined T/W values of AgCN and CuCN at ambient pressure ($245 \text{ K } k_B / W_{\text{AgCN}} = 0.14$ and $185 \text{ K } k_B / W_{\text{CuCN}} = 0.11$, cf. Fig. 2 **h**), is close to the T/W_0 scale of the theoretical data ($(k_B T_{\text{QWL}}/W)_{\text{AgCN}} = 0.24$ and $(k_B T_{\text{QWL}}/W)_{\text{CuCN}} = 0.14$). Keeping in mind the general overestimation of the critical T/W_0 and U/W_0 related to the iterated perturbation theory, these values are in good consensus. Thus, in addition to the excellent agreement of the qualitative shape of the QWL, there is also quantitative accordance between the optical, transport and theoretical results. While there is quantitative consistency for AgCN and CuCN, the T/W range covered by EtMe is larger than inferred from the optically determined bandwidth. Note, however, that the rescaling of transport data involves considerable insecurity since the QWL reversal of EtMe is not captured by the data of Ref. [S15]. Having a complete data set would certainly improve the quantitative accordance for this compound. Nevertheless it is remarkable that, for AgCN and CuCN, both the T/W and U/W scales agree well with the scaled transport results and DMFT calculations, and also the ambient pressure position $(U/W)_{\text{EtMe}}$ shows quantitative agreement on the common U/W scale.

S3 Reflectivity, Optical Conductivity and Band Parameter Determination

Figs. S3 and S4 illustrate the determination of the optical conductivity from the reflectivity R along both in-plane crystal axes. The phase shift Φ of the complex reflectivity $r = \sqrt{R}e^{i\Phi}$ is computed from the broad-band $R(\omega)$ data using the Kramers-Kronig relations, which allows for direct calculation of the complex refractive index and conductivity [S16].

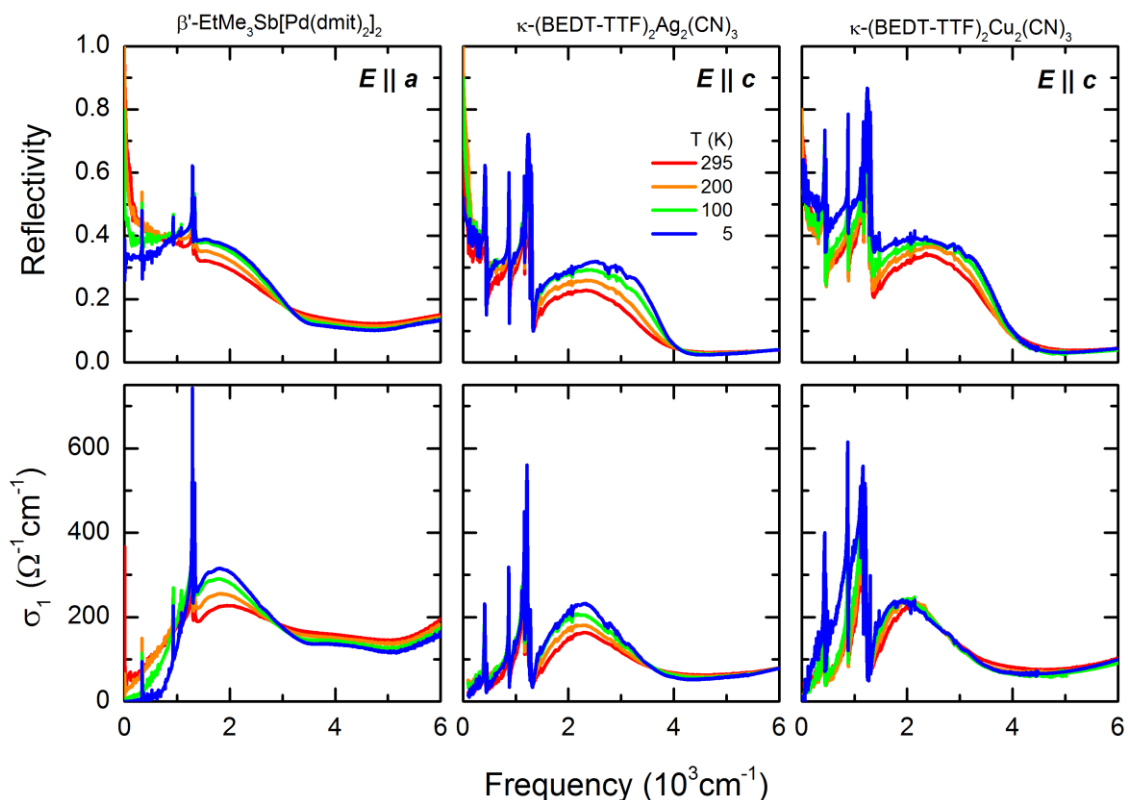


Figure S3. Optical reflectivity (upper panels) and conductivity (lower panels) along the in-plane direction with largest dc conductivity.

The optical conductivity of β' -EtMe₃Sb[Pd(dmit)₂]₂ ($E \parallel a$), κ -(BEDT-TTF)₂Ag₂(CN)₃ ($E \parallel c$) and κ -(BEDT-TTF)₂Cu₂(CN)₃ ($E \parallel c$) was calculated from the broad-band reflectivity data using the Kramers-Kronig relations. For convenience, only selected temperatures are plotted. Figure reproduced from Ref. [S31].

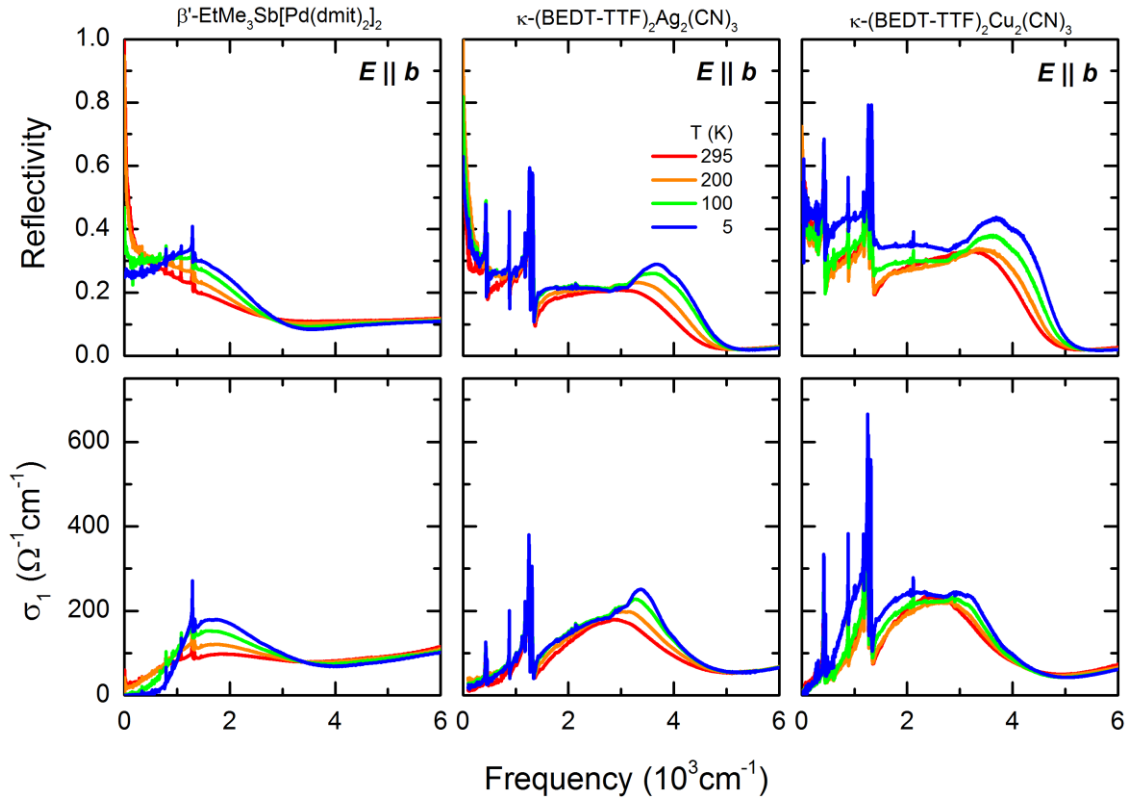


Figure S4. Optical reflectivity (upper panels) and conductivity (lower panels) along the in-plane direction with lowest dc conductivity.

The side band occurring for $E \parallel b$ in κ -(BEDT-TTF)₂Ag₂(CN)₃ and κ -(BEDT-TTF)₂Cu₂(CN)₃ results from intra-dimer excitations. Apart from the absolute values, phonons and molecular vibrations, the low-frequency optical conductivity shows qualitatively similar properties and temperature dependencies as for $E \parallel c$ (Fig. S3). Also for β' -EtMe₃Sb[Pd(dmit)₂]₂ the physical properties are the same for $E \parallel a$ and $E \parallel b$. Figure reproduced from Ref. [S31].

In Fig. S5 we plot the temperature-dependent optical conductivity $\sigma_1(\omega)$ for both in-plane polarizations of the three compounds under inspection, EtMe, AgCN and CuCN. In their overall appearance, the spectra are very similar for both polarizations with the Mott-Hubbard band around 2000 cm^{-1} . In the two κ -salts, however, the peak splits into a low- and high-energy part for the polarization $E \parallel b$. The latter corresponds to intra-dimer excitations while the former one is related to the charge transfer between the dimers; due to strong Coulomb repulsion the conduction band is split into the lower and upper Hubbard bands with transitions between them around 2000 cm^{-1} [S1,S5,S18]. Due to the overlapping features, the determination of ω_{max} of the inter-dimer part was less accurate than for the c -direction where the intra-dimer excitations are

less pronounced. In the case of EtMe the intra-dimer excitation band appears at much higher frequencies (around 4000 cm^{-1} for $E \parallel a$) because of its stronger dimerization.

Let us now consider the uncertainty in determining the Coulomb repulsion U and bandwidth W . While the band shape of EtMe is fairly smooth, particularly around the maximum and half-height, an intense vibrational feature around 1200 cm^{-1} complicates the determination of the half-height in the spectra of AgCN and, even more pronounced, for CuCN. While pure molecular vibrations exhibit a Lorentz shape, coupling to the electronic subsystem causes severe disturbance. For a phenomenological approach, the Fano model [S19] is commonly employed since it can capture the line shape very well. In strongly dimerized compounds, molecular

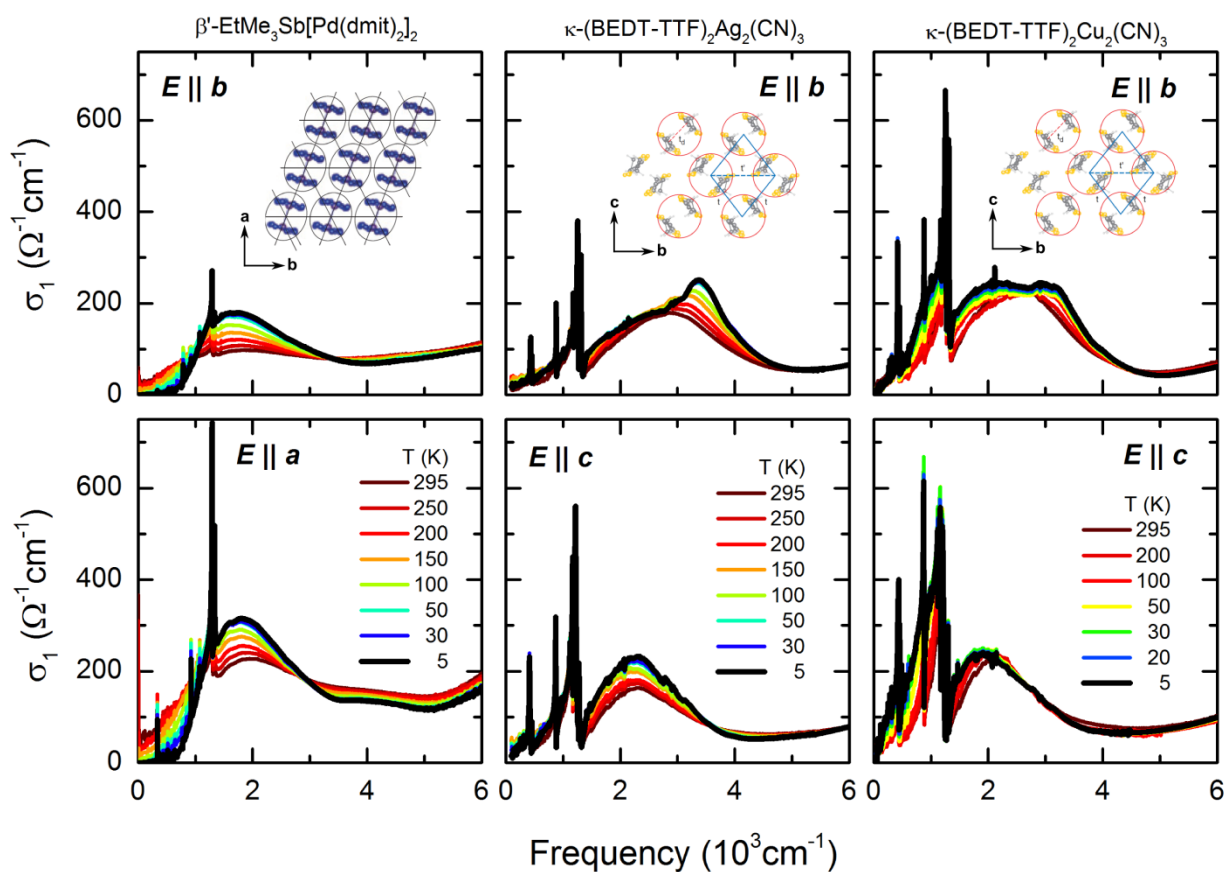


Figure S5. Optical conductivity of the studied compounds along both in-plane polarizations.

All spectra are dominated by the electronic transition from the lower to the upper Hubbard bands. The side band occurring for $E \parallel b$ in κ -(BEDT-TTF)₂Cu₂(CN)₃ and κ -(BEDT-TTF)₂Ag₂(CN)₃, and at 4000 cm^{-1} for $E \parallel a$ in β' -EtMe₃Sb[Pd(dmit)₂]₂, results from intra-dimer excitations. Apart from phonons and molecular vibrations, the low-frequency optical conductivity shows qualitatively similar properties and temperature dependencies for both polarizations. Figure reproduced from Ref. [S31].

vibrations may couple to the electronic subsystem, making fully symmetric A_g modes infrared-active [S20] and resulting in strong Fano-like features, as present in CuCN. In Fig. S6 we illustrate the behaviour of the rather narrow 875 cm^{-1} mode in CuCN. Due to the interaction of molecular vibrations and electronic background, the contributions to the optical conductivity do not simply add up: depending on the coupling, the phonon mode sitting on top of the electronic contribution can lead to a dip (antiresonance), or its contribution can be positive on one side and negative on the other side of the resonance frequency, as in the present case. The Fano parameter takes this interaction into account and the complex, asymmetric feature is described well.

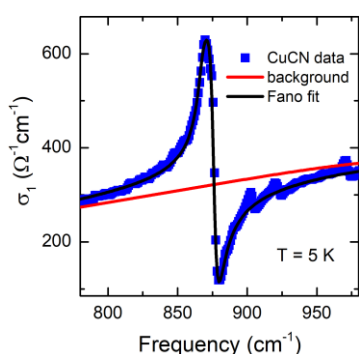


Figure S6. Fano fit of the 875 cm^{-1} mode. According to our ab-initio phonon calculations based on density functional theory [S21] this vibration involves the translations of the outer C=C bonds and breathing of the inner rings accompanied by the rocking of the terminal ethylene groups. Due to the coupling of the molecular vibrations to the electronic background, the mode acquires a Fano line shape. Figure reproduced from Ref. [S31].

Next, we disentangle the optical conductivity of CuCN (Fig. S7 **b**) and eliminate all vibrational contributions (cf. Refs. [S1] and [S22]); in particular the strong mode at 1200 cm^{-1} (black dotted line), that accounts for the pronounced dip in the spectrum, complicates the line shape. The conductivity of the Mott-Hubbard excitations is indicated in Fig. S7 **b** by the red dotted line. Higher-frequency processes, such as intra-dimer excitations and inter-band transitions, are shown by the green dotted line.

A consistent way to evaluate the bandwidth W is via the half width $\omega_{1/2}$ at half maximum $\frac{1}{2}\omega_{\max}$; we explicitly demonstrate it here for CuCN in Fig. S7 **b**. The low-energy wing is selected in order to rule out any effect by intra-dimer or inter-band excitations at higher frequencies. From the assignment in Fig. S7 we obtain $U = 1790\text{ cm}^{-1}$ and $W = 760\text{ cm}^{-1}$ yielding $U/W = 2.35 \pm 0.10$ for EtMe, as well as $U = 1830\text{ cm}^{-1}$ and $W = 1200\text{ cm}^{-1}$ yielding $U/W = 1.52 \pm 0.15$ for CuCN. We have chosen this method because it is the simplest and most robust procedure. Evaluating the full width at half maximum of the dotted red curve, for instance, we obtain $W = 850\text{ cm}^{-1}$ and 1180 cm^{-1} for EtMe and CuCN yielding slightly different values $U/W = 2.12$ and 1.55 , respectively, but not affecting the ordering in the phase diagram. Direct comparison of

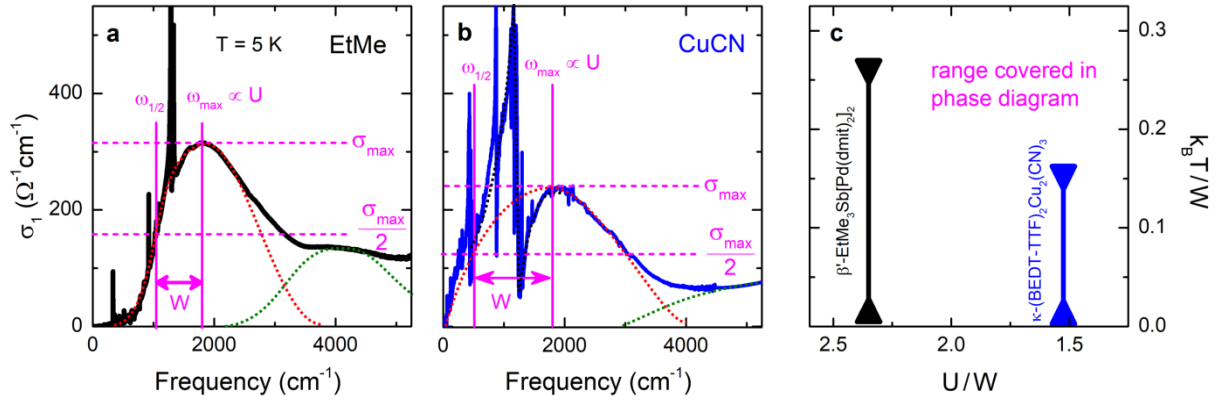


Figure S7. Determination of the Coulomb repulsion U and bandwidth W . **a,b** The optical conductivity is dominated by excitations between the Hubbard bands, described by the red dotted line; excitations of different origin at higher frequencies are indicated in green. The strong Fano contribution from the emv-coupled $A_g(\nu_2)$ molecular vibration mode (black dotted line in panel **b**) in the spectrum of CuCN is subtracted. The maximum in $\sigma_1(\omega)$ defines ω_{max} , which is a measure of the on-site Coulomb repulsion U . The bandwidth W is given by the half width $\omega_{1/2}$ at half maximum $\frac{1}{2}\omega_{\text{max}}$. **c** The effective correlations U/W for the compounds EtMe and CuCN determine their respective position in the phase diagram (cf. Fig. 2 **h**); the $k_B T/W$ range covered from 5 K up to room temperature is put in relation to the bandwidth indicated by the vertical extension of the bars.

panels **a** and **b** unequivocally confirms that the Mott-Hubbard excitation band in the spectrum of CuCN extends over a significantly broader frequency range than for EtMe. Therefore, CuCN has a larger bandwidth W and smaller correlation strength U/W than EtMe, placing CuCN closer to the metallic state, independent of the criterion used to extract the bandwidth.

We want to point out that the correlation strength U/W obtained from our optical data agrees well with *ab-initio* density functional theory and extended Hückel calculations [S9,S11,S13], as shown in Table 1. The theoretically derived bandwidth W and Coulomb repulsion U support the order in the phase diagram (EtMe-AgCN-CuCN), independently identifying CuCN as the compound with smallest correlation strength U/W , i.e. closest to the metallic state. Having the results of two independent methods (optics and theoretical estimates) makes our conclusions robust with respect to experimental uncertainties and remaining ambiguities in the analysis. Nevertheless, in Fig. S8 we indicate the individual error bars (dotted lines) of the U/W scale in the unified phase diagram arising from the band parameter determination using the optical spectra. The solid black line (shown in Fig. 4) is the envelope of the individual curves defining

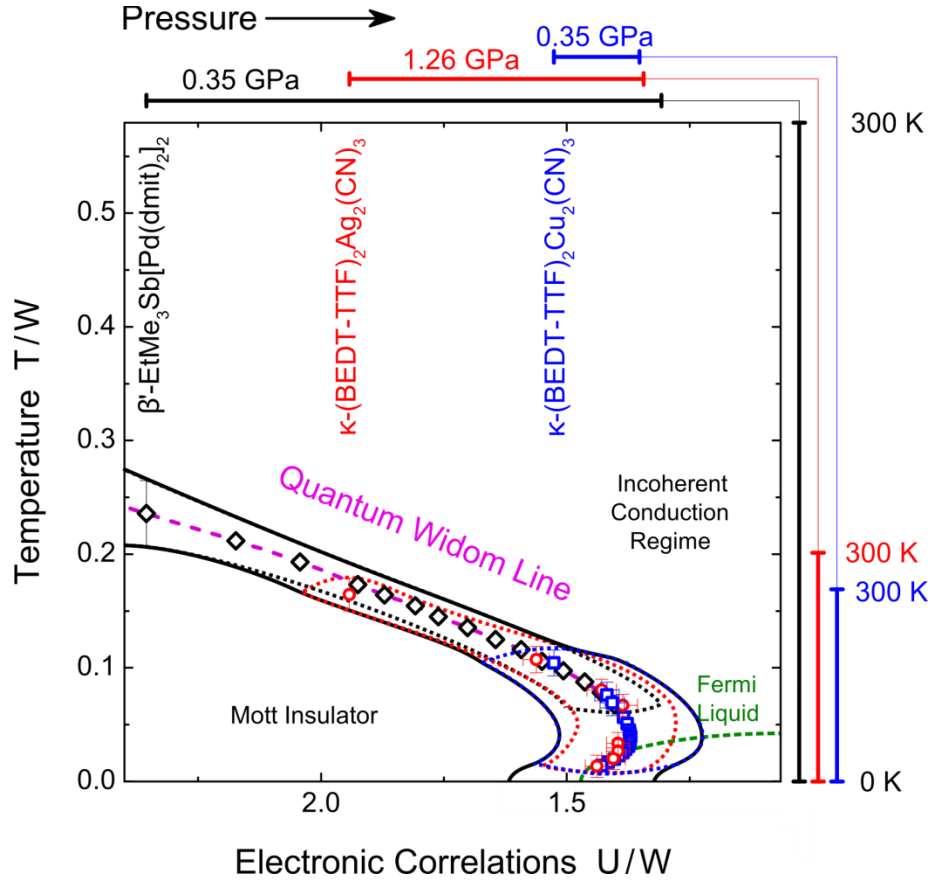


Figure S8. Experimental uncertainty of the unified phase diagram. The individual error bars upon extraction of U and W from the optical spectra are indicated in the respective colours by dotted lines. We also incorporated the uncertainty of the Widom line determination from temperature- (cf. Fig. S2) and pressure-dependent (cf. Fig. S13 c) dc transport according to section S2; the corresponding error bars are indicated as well. The solid black line is the overall uncertainty of the merged quantum Widom line, as shown in Fig. 4.

the overall uncertainty of the universal quantum Widom line, which also includes the uncertainty of the dc transport data discussed in section S2.

We also extracted the optical parameters for $E \parallel b$ which is plotted in Fig. S9 (empty symbols) together with the data from Fig. 2 e-g (filled symbols). Most importantly, the U/W_0 ratio in panel c shows qualitatively similar behaviour for both crystal directions. At low temperatures the thermal broadening of the bandwidth of EtMe and AgCN nicely follows the theoretically expected temperature dependence $\sqrt{W_0^2 + aT^2}$ [S8]. Additional smearing at elevated temperatures might be related to thermal population of low-frequency inter-molecular vibrations. At the lowest temperature, the absolute U/W value is slightly larger along $E \parallel b$ implying

stronger correlations and, thus, a position more *left* in the phase diagram. However, this anisotropy is substantially smaller than the insecurity in combining the Widom lines from transport measurements (see Section S2). The $(U/W)_{\text{exp}}$ values in Table 1 are taken from $E \parallel c$ due to the generally smaller error bar.

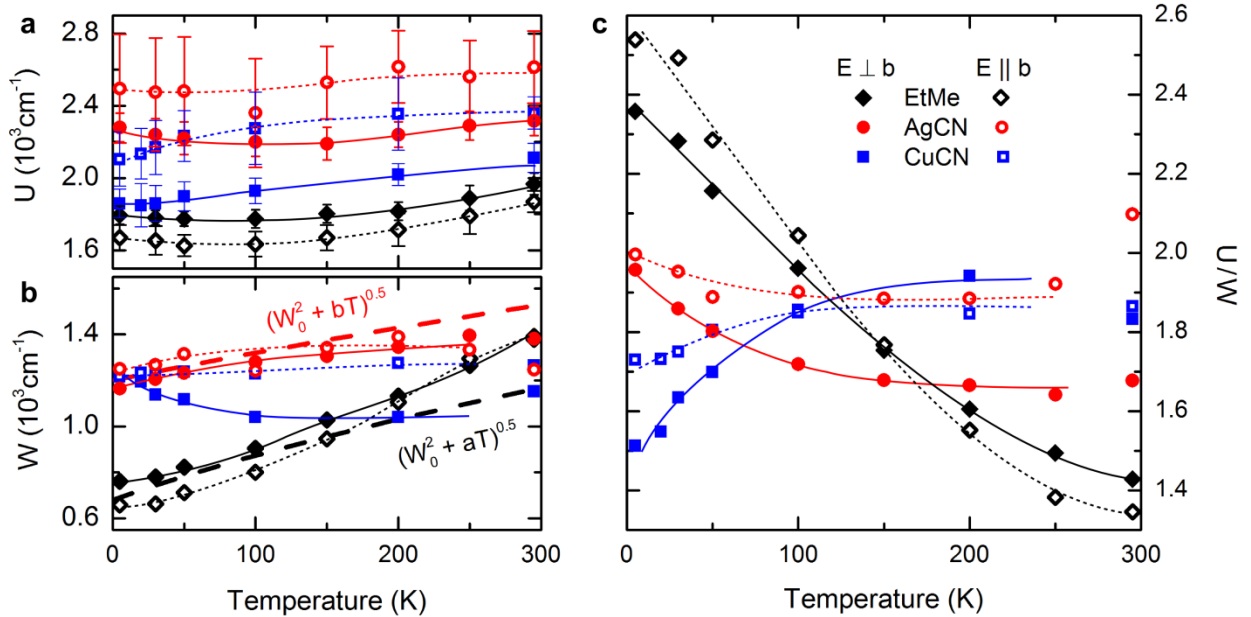


Figure S9. The optical parameters for both in-plane directions $E \parallel b$ (open symbols) and $E \perp b$ (solid symbols).

a, Temperature dependence of the maximum of the Mott-Hubbard band, which is proportional to U . **b**, Half-width at half-maximum of the Mott-Hubbard band $\omega_{\text{max}} - \omega_{1/2}$ proportional to W . The thick dashed lines correspond to a low-temperature approximation of the bandwidth broadening expected for pure thermal excitations [S8], which works reasonably well for β -EtMe₃Sb[Pd(dmit)₂]₂ and κ -(BEDT-TTF)₂Ag₂(CN)₃ up to $T \approx 150$ K. **c**, Ratio of these quantities U and W as a function of temperature (cf. Fig. 2 **e-g**). For both crystallographic directions we find a comparable T dependence. Due to overlapping inter- and intra-dimer excitations, the error bar is larger for $E \parallel b$, as indicated in panel **a**. Dashed and solid lines are guides to the eye. Figure reproduced from Ref. [S31].

S4 Low-Energy Electrodynamical Response

Metals and insulators are commonly defined according to the temperature-dependence of their resistivity. In a metal, the main changes of resistivity are related to the scattering rate γ , i.e. $\rho \propto \gamma \propto \sigma_{dc}^{-1}$, which increases with temperature and thus enhances (reduces) the resistivity (dc conductivity). For an insulator, the dominant contribution to charge transport is thermal activation; unlike in a metal the conductivity increases with temperature. As sketched in Fig. S10, a similar behaviour is expected for the low-frequency optical conductivity $\sigma_1(\omega, T)$ at energies well below the gap and scattering rate for insulators and metals, respectively.

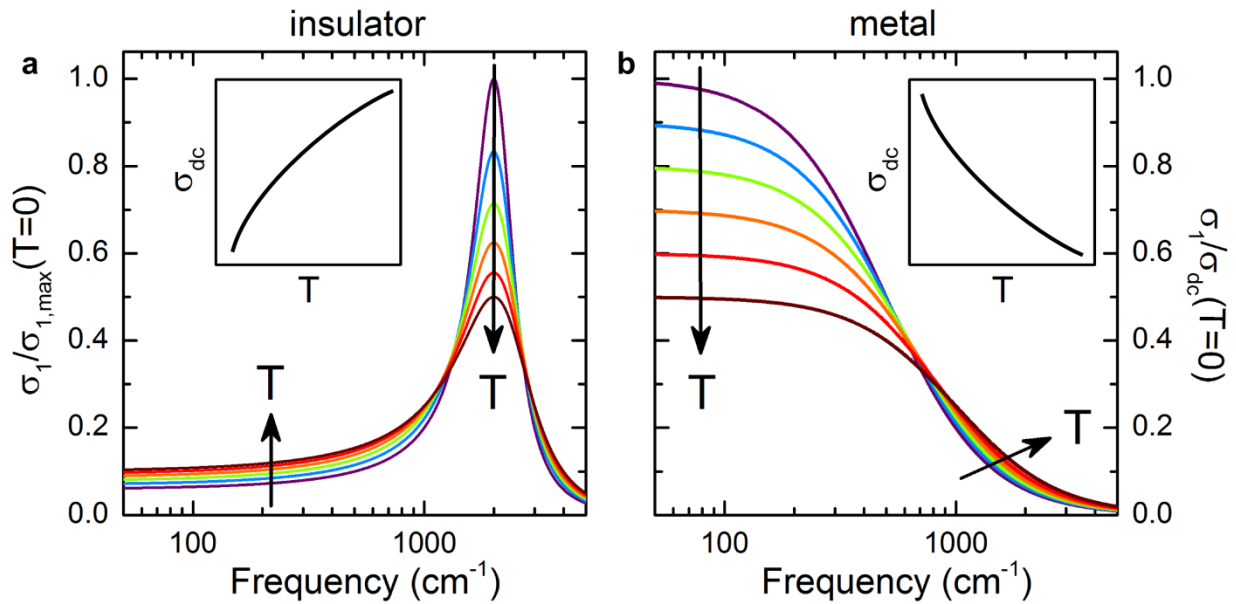


Figure S10. Characteristic spectroscopic and dc transport properties of insulators and metals. **a**, For an insulator, the band is located at finite frequency and the conductivity within the gap is very small. Upon increasing the temperature the spectral weight is shifted from the maximum to the (high- and) low-energy region causing an enhancement of the low-frequency conductivity. **b**, Since for a metal the Drude response is centred at $\omega = 0$, the low-energy contribution is suppressed with temperature. In the limit of very small frequencies the optical conductivity approaches the dc conductivity (insets), i.e. $\sigma_1(\omega = 0) = \sigma_{dc} = \rho^{-1}$. Thus, the low-energy spectral weight $SW(T)$ usually reveals a similar temperature evolution as $\sigma_{dc}(T)$. For an insulator the conductivity is thermally activated and thus increases with temperature; the opposite behaviour is found for a metal, where scattering impedes charge transport.

As intensely discussed in the main part, insulating behaviour is consistently found in the dc and low-frequency optical conductivity of EtMe and AgCN. For CuCN, however, the sub-gap spectral weight exhibits an anomalous increase upon cooling reminiscent of metallic behaviour despite insulating transport properties. We interpreted this anomaly as metallic fluctuations appearing in the vicinity of the insulator-metal phase boundary.

Although there is some anisotropy in the dc response and optical conductivity, the overall temperature dependence of charge transport is similar for both in-plane crystal axes. As shown in Fig. S11 a, in CuCN and AgCN the low-frequency optical conductivity is higher along the c -direction compared to $E \parallel b$, similar to the dc results [S23,S24]. This anisotropy is also expressed in the maximum position of the band (cf. Fig. S9 a); similar to the transport gap, U is larger for $E \parallel b$. This observation is explained by the fact that the bandwidth is largest along the c -direction. There is also small anisotropy for EtMe. The overall temperature evolution of the low-frequency response (Fig. S11 b,c), however, is robust and does not depend on the polarization which assures our assumption that we probe the intrinsic behaviour of the two-dimensional electron gas subject to strong correlations. Having two independent measurements strengthens our conclusion.

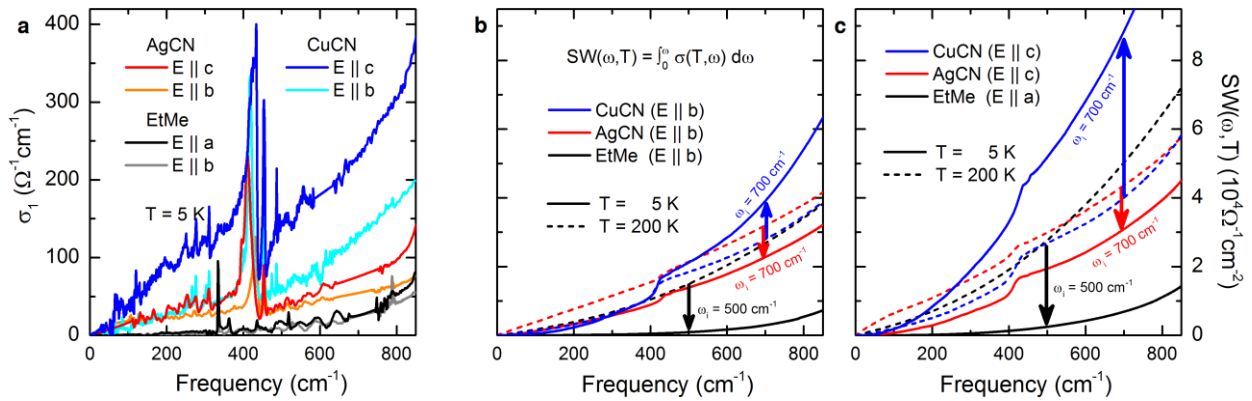


Figure S11. Polarization and temperature dependence of the low-frequency absorption.

a, Low-frequency conductivity of β -EtMe₃Sb[Pd(dmit)₂]₂, κ -(BEDT-TTF)₂Ag₂(CN)₃ and κ -(BEDT-TTF)₂Cu₂(CN)₃ for both polarizations shown at the lowest measured temperature.

b,c, Although the optical conductivity is anisotropic, there is no significant difference in the temperature dependence of the spectral weight SW , as indicated by the arrows. While it decreases for the former two compounds, it is enhanced for the latter one upon cooling, which is unexpected for an insulator (cf. Fig. S10). The arrows denote the frequency ω_i at which the temperature dependence of the spectral weight was compared in Figs. 3 and S15 a. Figure reproduced from Ref. [S31].

S5 Theoretical Calculations

In Fig. S12 we present the DOS (panel **a**) and optical conductivity (panel **b**) calculated by dynamical mean-field theory (DMFT) with the continuous time quantum Monte Carlo (CTQMC) impurity solver. As expected, and in agreement with the experimental spectra presented in Figs. 2 and S5, the maximum of $\sigma_1(\omega)$ shifts to higher energies as U increases. Importantly, the asymmetric shape of the Mott-Hubbard band observed in experiment is nicely reproduced. As shown in the inset of **b**, the maximum position of the optical conductivity is related linearly to the Coulomb repulsion U establishing our approach to extract the electronic interactions from the experimentally observed Mott-Hubbard band. The theoretical σ_1 scale is

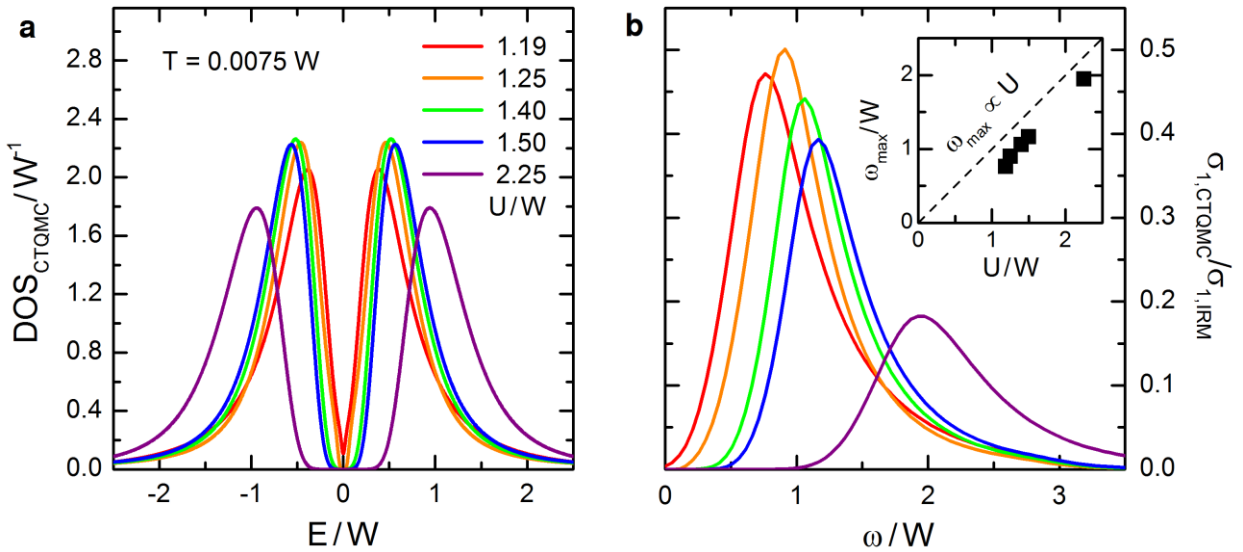


Figure S12. Density of states and optical conductivity calculated by dynamical mean-field theory (DMFT) with the continuous time quantum Monte Carlo (CTQMC) impurity solver.

The asymmetric shape of the Mott-Hubbard bands observed in our optical experiments (Fig. 2) is reproduced both in the DOS (**a**) and conductivity σ_1 (**b**) for different correlation strength U/W as indicated. The calculated optical conductivity is plotted in units of the Ioffe-Regel-Mott limit. The assumed $T/W = 0.0075$ corresponds to the low-temperature limit of our experiments. *Inset:* The linear relation between the maxima of optical conductivity and the Coulomb repulsion U reassures our analysis based on Fig. 2 **d**. Note, that due to the implicit assumptions of the theoretical model, the band edge is generally much steeper than in the materials under study. Here we utilized a Bethe lattice, while a triangular lattice was assumed for the iterated perturbation theory applied in Fig. 1 **a**, leading to different U/W values. Figure reproduced from Ref. [S31].

calculated in units of the Ioffe-Regel-Mott (IRM) limit $\sigma_{1,IRM} = e^2/(hd)$, where h is Planck's constant and d the inter-layer distance, which allows for quantitative comparison with our experimental data. Here, the IRM limit is around $210 \Omega^{-1}\text{cm}^{-1}$ for EtMe and $260 \Omega^{-1}\text{cm}^{-1}$ for the two κ -compounds [S10,S12,S25]. Thus, the experimental values are reproduced by our CTQMC calculations up to the same order of magnitude.

Note, that we used CTQMC on a Bethe lattice for the evaluation of the DOS and optical conductivity shown here, while the determination of the quantum Widom line shown in Fig. 1 a is based on iterated perturbation theory on the triangular lattice. As a result, the absolute values of U/W_0 might have an offset and different critical ratio at the Mott MIT; the general Mott physics, however, is captured by both approaches, as demonstrated in Ref. [S26].

S6 Mott Physics Above the Antiferromagnetic State in κ -(BEDT-TTF)₂Cu[N(CN)₂]Br_xCl_{1-x}

In the following, the quantum spin liquids are compared to the less-frustrated κ -(BEDT-TTF)₂Cu[N(CN)₂]Br_xCl_{1-x} series (abbreviated κ -Br_xCl_{1-x}) that shows magnetic order in the insulating state at low temperatures. While $T_N \approx 25$ K for $x = 0$ and $x = 0.4$, the compound with $x = 0.7$ is subject to an insulator-metal transition at $T_{MI} \approx 50$ K and becomes superconducting below $T_c \approx 12$ K [S1,S3,S4].

In Fig. S13 a we plot the phase diagram of the three κ -Br_xCl_{1-x} compounds based on their transport [S15,S4] and optical properties [S1,S3]. Due to similar bandwidth we use the same temperature and pressure scale as for CuCN and indicate the respective positions for each compound. At elevated temperatures Mott physics is dominant and the κ -Br_xCl_{1-x} compounds follow the same QWL (black line) as CuCN. At low temperatures, however, antiferromagnetic (AFM) order forms, causing a different behaviour than in the QSL compound. In particular, the Pomeranchuk-like back-bending of the QWL (open white squares indicate the phase boundary of CuCN) is suppressed by antiferromagnetic fluctuations such that the insulator-metal boundary (dashed pink) acquires a negative slope close to the AFM state. Note that in the presence of strong geometrical frustration in CuCN the metallic state is stabilized with respect to the Mott state up to larger correlations U/W , i.e. smaller pressure, than in the less-frustrated κ -Br_xCl_{1-x} series. Thus, AFM and its fluctuations suppress the Fermi liquid and affect thermodynamics more strongly than the pure interplay of charge excitations and Coulomb repulsion.

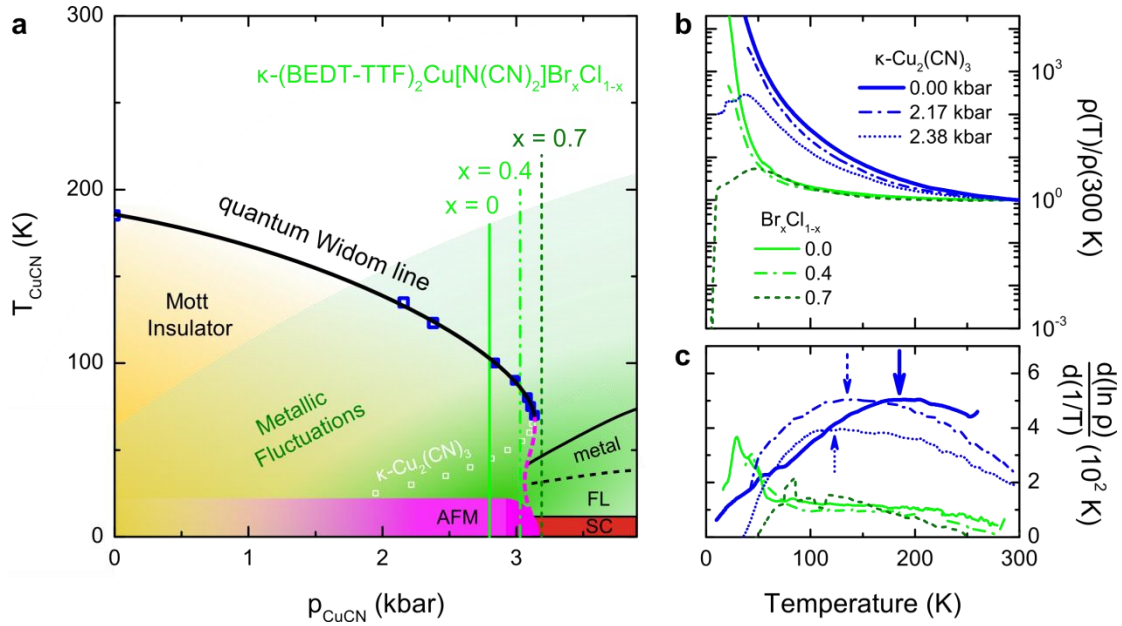


Figure S13. Phase diagram the antiferromagnetic κ -(BEDT-TTF) $_2$ Cu[N(CN) $_2$]Br $_x$ Cl $_{1-x}$.

a, The black line corresponds to the common high-temperature quantum Widom line of κ -(BEDT-TTF) $_2$ Cu $_2$ (CN) $_3$ (blue squares, Figs. 4, S1) and κ -(BEDT-TTF) $_2$ Cu[N(CN) $_2$]Br $_x$ Cl $_{1-x}$. The solid, dashed-dotted and dashed green lines refer to the ambient pressure positions of the compounds with $x = 0, 0.4$ and 0.7 , respectively [S1,S3,S4,S15]. As indicated in semi-transparent green colour, metallic fluctuations appear both in the Mott state and in the incoherent regime above and right of the quantum Widom line (see discussion of Fig. S15 a). Since geometrical frustration is much smaller than in κ -(BEDT-TTF) $_2$ Cu $_2$ (CN) $_3$, antiferromagnetic (AFM) order sets in below $T_N \approx 25$ K for $x \leq 0.4$ as indicated in pink. The associated antiferromagnetic fluctuations suppress the back-bending of the quantum Widom line and cause a negative slope of the insulator-metal boundary in the vicinity of the ordered state (dashed pink line). The open white squares indicate how the low-temperature phase boundary would form in absence of AFM, realized by the geometrically frustrated κ -(BEDT-TTF) $_2$ Cu $_2$ (CN) $_3$. Thus, magnetic order suppresses the metallic phase up to higher pressure (i.e. smaller U/W ratio) compared to a pure Mott insulator. **b**, The resistivity data reveal that increasing the Br-content effectively enhances the bandwidth leading to metallic and superconducting behaviour at low temperatures. We also plot the pressure-dependent resistivity of CuCN (blue) for $p = 0, 2.17$ and 2.38 kbar. **c**, The logarithmic resistivity derivative of the κ -(BEDT-TTF) $_2$ Cu[N(CN) $_2$]Br $_x$ Cl $_{1-x}$ compounds is qualitatively different from the quantum spin liquids. A pronounced peak occurs around T_N . The transport gap maximum of CuCN (open blue squares in **a**) shifts to lower temperature upon pressure. Figure reproduced from Ref. [S31].

The transport properties shown in Fig. S13 **b** reveal the typically smaller resistivity of $\kappa\text{-Br}_x\text{Cl}_{1-x}$ in accordance with the location much closer to the metallic state due to smaller correlations U/W . This effect is seen very clearly in frame **c** as the transport gap is significantly smaller than in CuCN. In the vicinity of its reversal point the QWL acquires a nearly vertical slope over a broad temperature range (for $x = 0$, see Fig. 1 **e** from Ref. [S15]). Hence, the contribution to the transport gap related with Mott physics manifests as a broad plateau above 50 K. The bandwidth tuning effect becomes obvious as (i) the size of the transport gap is much smaller than in the three quantum spin liquid compounds under study with stronger correlations, and (ii) the high-temperature tail of the plateau is suppressed for larger Br-content x . When entering the AFM state, however, the resistance shoots up drastically which expresses as a sharp maximum centered at T_N in the logarithmic derivative. The onset happens well above the magnetic transition, indicating magnetic fluctuations for $T_N < T < 50\text{K}$.

To compare the electrodynamic properties in the context of Mott physics, we confine ourselves to a temperature right above the onset of magnetic fluctuations. In Fig. S14 **a** we plot the optical conductivity of the three quantum spin liquids and the three $\kappa\text{-Br}_x\text{Cl}_{1-x}$ compounds at $T = 50\text{ K} > T_N$. To facilitate comparison, we renormalized the Mott-Hubbard band to the maximum conductivity $\sigma_{1,\text{max}}$ and frequency ω_{max} , respectively. Additionally, we smoothed the data as the frequency shift moves the vibrational features differently for each compound making the picture confusing. As a general trend, the in-gap conductivity is enhanced for smaller correlations. The optical conductivity calculated by DMFT shown in Fig. S12 **b** was normalized the same way and, similarly, exhibits a pronounced broadening of the band for reduced U/W (Fig. S14 **b**).

In Fig. S15 **a** we plot the spectral weight (SW) integrated up to a cut-off frequency $\omega_i < (U - W)$ for both in-plane directions of the quantum spin liquids, cf. Fig. 3 **d**. The overall temperature evolution is the same for both polarizations, in line with the findings for the spin liquid compounds. Performed the corresponding SW analysis on the $\kappa\text{-Br}_x\text{Cl}_{1-x}$ series ($\omega_i = 700\text{ cm}^{-1}$) we conclude that these materials show a similar non-thermal enhancement of the in-gap absorption like CuCN. Note, that for $T > 50\text{ K}$ the low-frequency optical conductivity measured by the integrated SW increases upon cooling although the dc resistivity (Fig. S13 **b**) resembles an insulating behaviour. There is only little difference between $x = 0$ and 0.4 on the one hand, as both are located in the Mott insulating region, and the compound with $x = 0.7$ on the other hand, which is presumably in the incoherent regime above $T_{\text{MI}} \approx 50\text{ K}$. We conclude that the

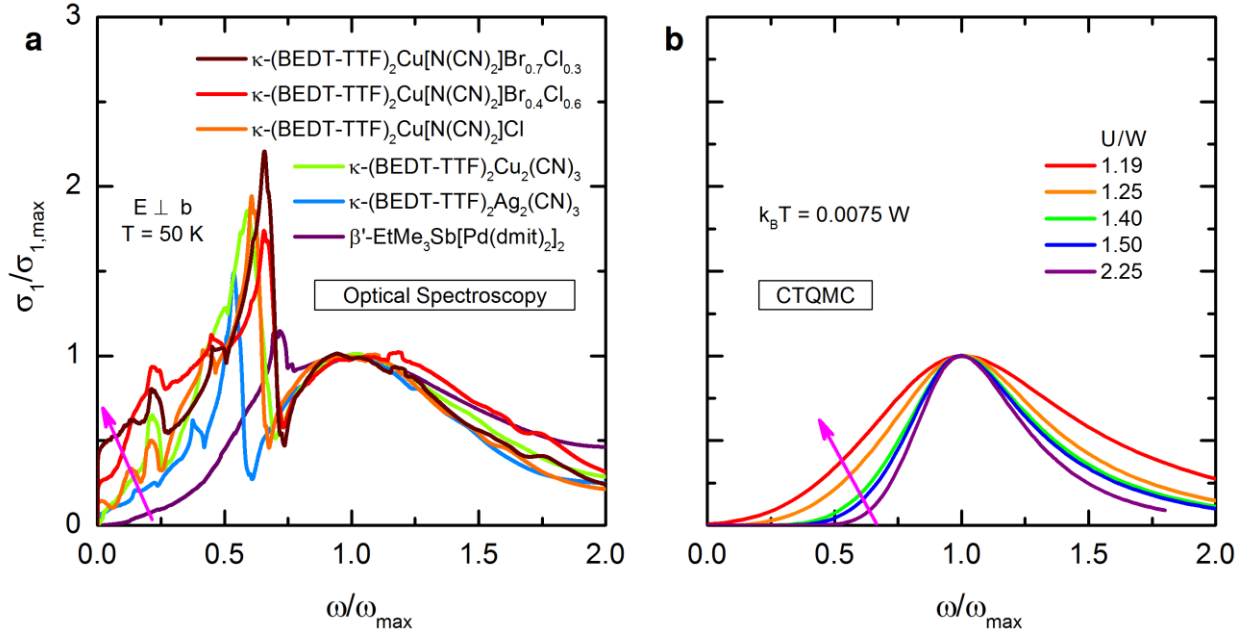


Figure S14. Similar bandwidth-tuning effect on low-frequency absorption in experiment and theory.

a, Normalized optical conductivity of two-dimensional Mott insulators with different effective correlations U/W : the data are smoothed and normalized to the maximum conductivity σ_{\max} of the Mott-Hubbard band and the corresponding frequency ω_{\max} . The $T = 50$ K data for β -EtMe₃Sb[Pd(dmit)₂]₂, κ -(BEDT-TTF)₂Ag₂(CN)₃ and κ -(BEDT-TTF)₂Cu₂(CN)₃ are complemented by spectra of κ -(BEDT-TTF)₂Cu[N(CN)₂]Br_xCl_{1-x} with $x = 0$ and 0.4 above their magnetic order ($T_N = 25$ K), as well as $x = 0.7$ [S1,S3]. **b**, Bandwidth tuning affects the experimental optical conductivity in a similar way as predicted by theoretical calculations based on the DMFT method (cf. Fig. S12 **b**). Most important is the enhancement of the low-frequency conductivity when correlations are reduced, as indicated by the magenta arrows. Figure reproduced from Ref. [S31].

non-thermal enhancement of the SW is caused by metallic quantum fluctuations that appear on both sides of the quantum Widom line in the vicinity of the metallic phase, i.e. in the Mott state and the incoherent regime, as pointed out in Fig. S13 **a**. This precursor of coherent quasiparticles is a robust feature observed in Mott insulators with and without magnetic order, and varying degree of geometrical frustration. Also, the effect of antiferromagnetism can be clearly separated since for $x = 0$ and $x = 0.4$ the spectral weight rapidly drops below T_N when the antiferromagnetic gap opens. Apparently, charge fluctuations are suppressed more strongly by AFM order than by the intrinsic Coulomb interactions of the Mott state.

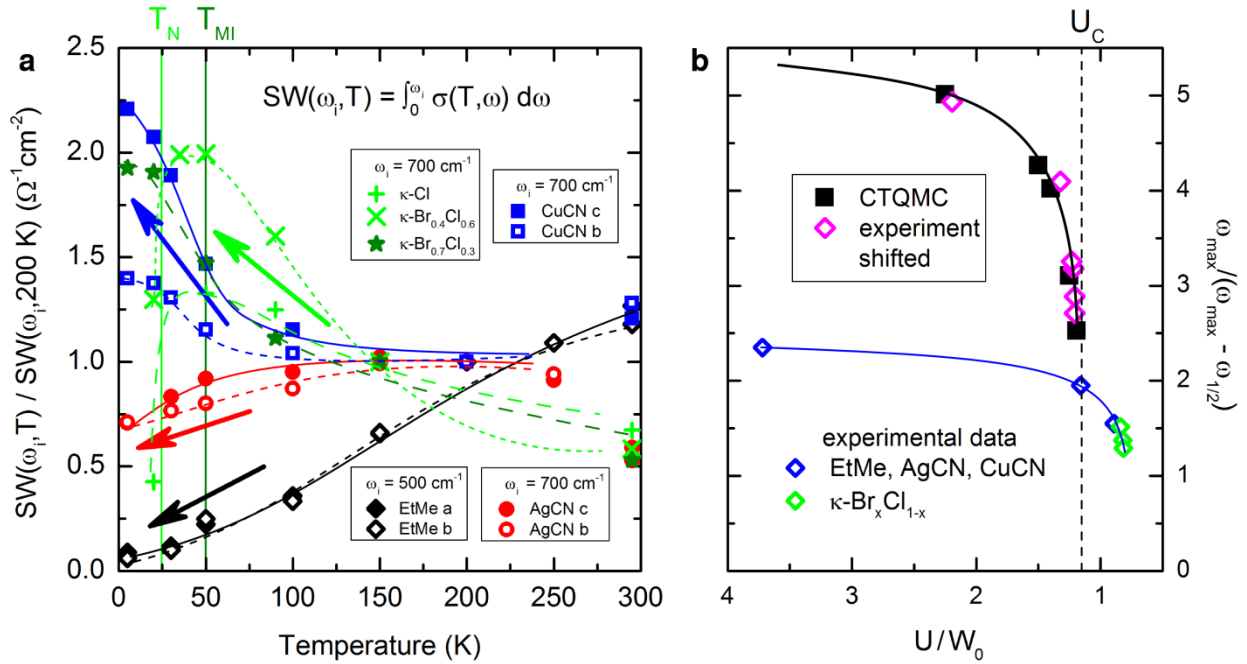


Figure S15. Optical parameters compared between quantum spin liquids, antiferromagnetic insulators and dynamical mean-field theory results.

a, Temperature evolution of the spectral weight (SW) of the three quantum spin liquid compounds $\beta\text{-EtMe}_3\text{Sb}[\text{Pd}(\text{dmit})_2]_2$, $\kappa\text{-(BEDT-TTF)}_2\text{Ag}_2(\text{CN})_3$ and $\kappa\text{-(BEDT-TTF)}_2\text{Cu}_2(\text{CN})_3$. In extension to Fig. 3 **d**, both polarizations are plotted yielding similar temperature evolution. In addition, the SW of the antiferromagnetic Mott insulators from the $\kappa\text{-(BEDT-TTF)}_2\text{Cu}[\text{N}(\text{CN})_2]\text{Br}_x\text{Cl}_{1-x}$ series is included [S1,S3]. Above T_N these systems behave similarly as $\kappa\text{-(BEDT-TTF)}_2\text{Cu}_2(\text{CN})_3$ supporting our conclusion of the non-thermal low-energy absorption. As magnetic order sets in for $x = 0$ and $x = 0.4$, the spectral weight drastically drops due to the opening of the antiferromagnetic gap. **b**, Correlation dependence of the maximum of the optical conductivity with respect to its width of the lowest-temperature data from Figs. 2 and S14 (blue) contrasted to the $\kappa\text{-(BEDT-TTF)}_2\text{Cu}[\text{N}(\text{CN})_2]\text{Br}_x\text{Cl}_{1-x}$ series (green) and the DMFT results (black) from Fig. S12 **b**. Note the reversed axis of ordinates. The discrepancy between experiment and theory is most likely due to several assumptions of the model. Still, the trends agree very well: i.e. the experimental data can be rescaled to match exactly with theory (magenta symbols). Hence, we conclude that the underlying Mott physics is reproduced reasonably well by the CTQMC calculations. Figure reproduced from Ref. [S31].

S7 Experiment vs. Theory

Finally, we compare the band shape of the experimentally determined optical conductivity with the spectra calculated by the DMFT method in section S5. Fig. S15 **b** shows the ratio of the maximum position ω_{\max} of the Mott-Hubbard band and the half-width on its low-frequency wing $\omega_{\max} - \omega_{1/2}$, i.e. U/W as determined in Fig. 2 **h**, with respect to the degree of electronic correlations U/W_0 . For the experiment, we plot the lowest temperature values of Fig. S9 versus the theoretically calculated (DFT, extended Hückel) U/W_0 values from Table S1. The $\kappa\text{-Br}_x\text{Cl}_{1-x}$ data were extracted similarly as for the quantum spin liquids. At first glance, there is a quantitative discrepancy between experimental and theoretical data since, apparently, the theoretical bands are narrower and the calculations imply the onset of Mott insulating behaviour at a larger U_C/W_0 . However, there are many assumptions of the theoretical model that may cause deviations of the absolute values, such as the Bethe lattice instead of a triangular lattice, the dimer approximation, electron-lattice coupling, screening etc. Therefore, it is reasonable to shift the experimental curve to a different onset U_C/W_0 and rescale the absolute values. As the result of such a transformation, the experimental data match perfectly with the theoretical ones and their curvature compares very well. Hence, our theoretical model that only includes the charge dynamics of the Mott insulator qualitatively reproduces the electrodynamic response of our optical spectroscopy results.

S8 Comparison with Transition-Metal Oxides

In Fig. S16 **a**, we illustrate the experimentally covered ranges in the unified phase diagram shown in Fig. 4, including our own experiments on the three frustrated Mott insulators (optics and pressure-dependent dc transport) as well as the data reported in Refs. [S13,S15]. For comparison, we add the data of $(\text{V}_{1-x}\text{Cr}_x)_2\text{O}_3$ which exhibits a transition from a paramagnetic metal to a Mott insulator upon chromium substitution. In Fig. S16 **b** the pressure and temperature dependence of the phase transition is plotted as obtained from dc transport measurements at variable pressure [S27]. From optical experiments [S28,S29,S30] it can be estimated that the bandwidth is approximately higher by a factor of 25 compared to EtMe; the Coulomb repulsion U is around 2.6 eV. Performing the proper scaling, we can match the phase boundary of vanadium sesquioxide with the universal QWL, covering a significantly smaller region in the phase diagram. Note that $T = 300$ K on the EtMe temperature scale correspond to several 10^3 or even 10^4 K for vanadium oxides, cuprates or similar materials, which is well above their melting points. Thus, the small bandwidth of the organic compounds allows us to

reach a temperature regime far beyond the grasp of transition-metal oxides, giving unique insight into incoherent conduction processes outside the realm of quasiparticles.

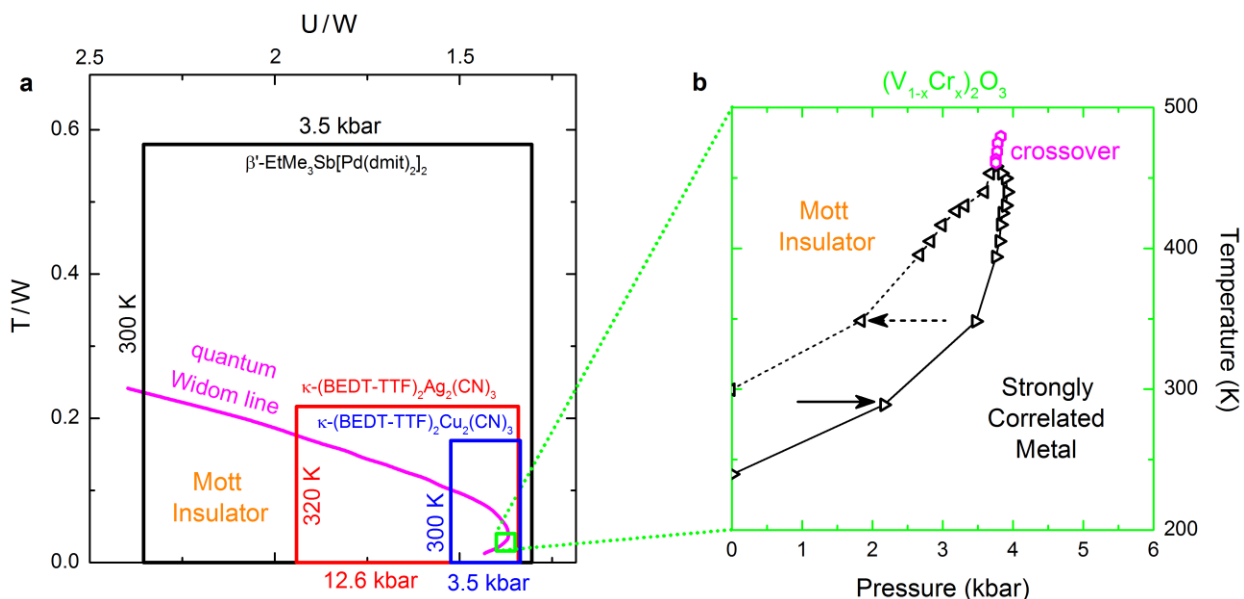


Figure S16. Range of experimental exploration in the unified phase diagram.

a, Experiments on various compounds cover the unified phase diagram of Fig. 4 to a different degree. We illustrate the respective T/W and U/W ranges by coloured frames (cf. Section S2). As the bandwidth increases in the order β -EtMe₃Sb[Pd(dmit)₂]₂ (black) - κ -(BEDT-TTF)₂Ag₂(CN)₃ (red) - κ -(BEDT-TTF)₂Cu₂(CN)₃ (blue), the corresponding range is successively reduced, both vertically and horizontally. **b**, Experimentally accessible phase boundary of $(V_{1-x}Cr_x)_2O_3$ as a function of pressure and temperature (reproduced from Ref. [S27]). By including these data in panel **a** by the green frame, it becomes obvious that a much smaller region is covered despite the larger temperature and pressure scales. This is a direct consequence of the larger energy scales, U and W , in transition-metal oxides. Figure reproduced from Ref. [S31].

References

- [S1] Faltermeier, B. *et al.* Bandwidth-controlled Mott transition in κ -(BEDT-TTF)₂Cu[N(CN)₂]Br_xCl_{1-x}: Optical studies of localized charge excitations. *Phys. Rev. B* **76**, 165113 (2007).
- [S2] Merino, J., Dumm, M., Drichko, N., Dressel, M. & McKenzie, R. H., Quasiparticles at the Verge of Localization near the Mott Metal-Insulator Transition in a Two-Dimensional Material. *Phys. Rev. Lett.* **100**, 086404 (2008).
- [S3] Dumm, M. *et al.* Bandwidth-controlled Mott transition in κ -(BEDT-TTF)₂Cu[N(CN)₂]Br_xCl_{1-x}: Optical Studies of Correlated Carriers. *Phys. Rev. B* **79**, 195106 (2009).
- [S4] Yasin, S. *et al.* Transport studies at the Mott transition of the two-dimensional organic metal κ -(BEDT-TTF)₂Cu[N(CN)₂]Br_xCl_{1-x}. *Eur. Phys. J. B* **79**, 383-390 (2011).
- [S5] Ferber, J., Foyevtsova, K., Jeschke, H. O. & Valentí, R. Unveiling the microscopic nature of correlated organic conductors: The case of κ -(ET)₂Cu[N(CN)₂]Br_xCl_{1-x}. *Phys. Rev. B* **89**, 205106 (2014).
- [S6] Hubbard, J. Electron Correlations in Narrow Energy Bands. *Proc. R. Soc. London, Ser. A* **281**, 401-419 (1964).
- [S7] Vollhardt, D., Investigation of Correlated Electron Systems Using the Limit of High Dimensions, in: *Correlated Electron Systems*, edited by V.J.Emery (World Scientific, Singapore, 1992).
- [S8] Fratini, S. & Ciuchi, S. Spectral properties and isotope effect in strongly interacting systems: Mott-Hubbard insulator versus polaronic semiconductor. *Phys. Rev. B* **72**, 235107 (2005).
- [S9] Kandpal, H.C., Opahle, I., Zhang, Y.-Z., Jeschke, H.O. & Valentí, R. Revision of Model Parameters for κ -Type Charge Transfer Salts: An Ab Initio Study. *Phys. Rev. Lett.* **103**, 067004 (2009).
- [S10] Kato, R., Fukunaga, T., Yamamoto, H.M., Ueda, K., & Hengbo, C. Crystal Structure and Band Parameters of Mixed Crystals Derived from Quantum Spin Liquid β' -EtMe₃Sb[Pd(dmit)₂]₂ (dmit: 1,3-dithiole-2-thione-4,5-dithiolate). *Phys. Stat. Solidi B* **249**(5), 999-1003 (2012).
- [S11] Kato, R., & Hengbo, C. Cation Dependence of Crystal Structure and Band Parameters in a Series of Molecular Conductors, β' -(Cation)[Pd(dmit)₂]₂ (dmit: 1,3-dithiole-2-thione-4,5-dithiolate). *Crystals* **2**, 861-874 (2012).
- [S12] Hiramatsu, T. *et al.* κ -(ET)₂Ag₂(CN)₃: Rational Design of Organic Quantum Spin Liquid Candidate Using Key-Keyhole Strategy. to be published in *Cryst. Growth Design* (2017).
- [S13] Shimizu, Y. *et al.* Pressure-Tuned Exchange Coupling of a Quantum Spin Liquid in the Molecular Triangular Lattice κ -(ET)₂Ag₂(CN)₃. *Phys. Rev. Lett.* **117**, 107203 (2016).
- [S14] Itou, T., Oyamada, A., Maegawa, S. Tamura, M. & Kato, R. Quantum spin liquid in the spin-1/2 triangular antiferromagnet EtMe₃Sb[Pd(dmit)₂]₂. *Phys. Rev. B* **77**, 104413 (2008).
- [S15] Furukawa, T., Miyagawa, K., Taniguchi, H., Kato, R. & Kanoda, K. Quantum criticality of Mott transition in organic materials. *Nature Phys.* **11**, 221-224 (2015).
- [S16] Dressel, M. & Grüner, G. *Electrodynamics of Solids* (Cambridge University Press, Cambridge, 2002).

- [S17] Kurosaki, Y., Shimizu, Y., Miyagawa, K., Kanoda, K. & Saito, G. Mott Transition from a Spin Liquid to a Fermi Liquid in the Spin-Frustrated Organic Conductor κ -(ET)₂Cu₂(CN)₃. *Phys. Rev. Lett.* **95**, 177001 (2005).
- [S18] Nakamura, Y., Hiramatsu, T., Yoshida, Y., Saito, G. & Kishida, H. Optical Properties of a Quantum Spin Liquid Candidate Material, κ -(BEDT-TTF)₂Ag₂(CN)₃. *J. Phys. Soc. Jpn.* **86**, 014710 (2017).
- [S19] Fano, U. Effects of Configuration Interaction on Intensities and Phase Shifts. *Phys. Rev.* **124**, 1866 (1961).
- [S20] Rice, M.J. Towards the experimental determination of the fundamental microscopic parameters of organic ion-radical compounds. *Solid State Commun.* **31**, 93 (1979).
- [S21] Dressel, M. *et al.* Lattice vibrations of the charge-transfer salt κ -(BEDT-TTF)₂Cu₂(CN)₃: Comprehensive explanation of the electrodynamic response in a spin-liquid compound. *Phys. Rev. B* **93**, 081201 (2016).
- [S22] Elsässer, S. *et al.* Power-law dependence of the optical conductivity observed in the quantum spin-liquid compound κ -(BEDT-TTF)₂Cu₂(CN)₃. *Phys. Rev. B* **86**, 155150 (2012).
- [S23] Pinterić, M. *et al.* Anisotropic Charge Dynamics in the Spin-Liquid Candidate κ -(BEDT-TTF)₂Cu₂(CN)₃. *Phys. Rev. B* **90**, 195139 (2014).
- [S24] Pinterić, M. *et al.* Anions effects on the electronic structure and electrodynamic properties of the Mott insulator κ -(BEDT-TTF)₂Ag₂(CN)₃. *Phys. Rev. B* **94**, 161105 (2016).
- [S25] Jeschke, H.O. *et al.* Temperature dependence of structural and electronic properties of the spin-liquid candidate κ -(BEDT-TTF)₂Cu₂(CN)₃. *Phys. Rev. B* **85**, 035125 (2012).
- [S26] Terletska, H., Vučičević, J., Tanasković, D. & Dobrosavljević, V. Quantum Critical Transport near the Mott Transition. *Phys. Rev. Lett.* **107**, 026401 (2011)
- [S27] Limelette, P. *et al.* Universality and Critical Behaviour at the Mott Transition. *Science* **302**, 89-92 (2003).
- [S28] Qazilbash, M. M. *et al.* Electrodynamic of the vanadium oxides VO₂ and V₂O₃, *Phys. Rev. B* **77**, 115121 (2008).
- [S29] Perucchi, A., Baldassarre, L., Postorino, P. & S. Lupi, Optical properties across the insulator to metal transitions in vanadium oxide compounds. *J. Phys.: Condens. Matter* **21** 323202 (2009).
- [S30] Lo Vecchio, I. *et al.* Optical properties of V₂O₃ in its whole phase diagram, *Phys. Rev. B* **91**, 155133 (2015).
- [S31] Pustogow, A. Unveiling Electronic Correlations in Layered Molecular Conductors by Optical Spectroscopy. *PhD Thesis at University of Stuttgart*, 79-105 (2017).